FULL RESEARCH ARTICLE

Microstructure and mechanical properties of β-21S Ti alloy fabricated through laser powder bed fusion

Maria Argelia Macias-Sifuentes[1] · Chao Xu[2] · Oscar Sanchez-Mata[1] · Sun Yong Kwon[1] · Sila Ece Atabay[1] · Jose Alberto Muñiz-Lerma[1] · Mathieu Brochu[1]

Abstract

Metastable β-titanium alloys are attractive for their high strength-to-density ratio, good hardenability, excellent fatigue behavior, and corrosion resistance. Among these alloys, β-21S, with a composition of Ti–15Mo–3Nb–3Al–0.2Si (wt%), is known to offer improved elevated temperature strength, creep resistance, thermal stability, and oxidation resistance. In this study, laser powder bed fusion (PBF-LB) of β-21S and the effect of post-PBF-LB heat treatment were investigated to understand the relationship between the microstructure and the mechanical properties. The as-built (AB) alloy is primarily composed of β-phase, with columnar grains oriented along the build direction. The alloy AB presented a microhardness of 278 HV, a yield strength (YS) of 917 MPa, an ultimate tensile strength (UTS) of 946 MPa, and a ductility of 25.3% at room temperature (RT). Such properties are comparable to β-21S in solution treatment (ST) condition. Solution treatment and aging (STA) of the alloy precipitated the α-phase, increasing the microhardness to 380 HV, YS to 1281 MPa and UTS to 1348 MPa, while reducing the ductility to 6.5% at RT. The STA alloy presented a YS of 827 MPa, UTS of 923 MPa, and a ductility of 7.7%, at 450 °C. The thermal treatment applied to PBF-LB β-21S had a similar effect compared to β-21S fabricated by non-AM techniques. The properties obtained demonstrate that β-21S is a potential candidate for AM.

Keywords Laser powder bed fusion · Titanium β-21S · Microstructure · Mechanical properties

1 Introduction

AM is emerging as a complementary route to the traditional manufacturing processes to fabricate high complexity components. PBF-LB, one of the most studied processes among metal AM, uses powder feedstock which is selectively melted by a focused laser to form a characteristic part after melt pool solidification [1–4]. PBF-LB has raised attention due to its high degree of manufacturing freedom, its ability to produce lightweight intricate components [5, 6], and its energy-efficient and time-saving route [6, 7].

Metastable β-titanium alloys are attractive materials for aerospace applications due to their high strength-to-density ratio, good hardenability, excellent fatigue/crack-propagation behavior capabilities with processes such as cold strip rolling [8, 9]. Compared to other metastable β-titanium alloys, β-21S offers better oxidation resistance, it can retain its strength at higher temperatures [9–11], and has increased corrosion resistance [10, 12]. β-21S is an age hardenable metastable β-titanium alloy that has great forming capabilities, contains a balance of β-stabilizers which upon fast cooling from above β-transus, retains the β-phase [8, 13], and the formation of martensite at room temperature is inhibited. The β-phase retained is metastable at high temperature and is typically heat treated to precipitate the α-phase, to increase the strength and stabilize the microstructure of the alloy. Typical heat treatment involves solution treatment at temperatures above the β-transus (805 °C [14]) (known as β-solution treatment) followed by aging [8]. Aging at temperatures above the ω-solvus (350 °C [15]) will precipitate the α-phase within the grains and at the grain boundaries [13, 16] strengthening the alloy [17]. The selected heat treatment in this study is the standard STA for β-21S [18] with aging temperature above the ω-solvus. Agarwal et al. [19] and Huang et al. [4] studied the influence of different

✉ Mathieu Brochu
  mathieu.brochu@mcgill.ca

1 Mining and Materials Engineering, McGill University, Montreal, Canada

2 Department of Mechanical and Aerospace, Jilin University, Changchun, China

heat treatments on the microstructure of β-21S produced by non-AM processes in STA. With the standard heat treatment used in this study, they reported a microstructure consisting on fine α-phase in a β-matrix and on the grain boundaries. Huang et al. reported the α-phase is expected to precipitate with a volume percentage ranging between 20 and 33% [4].

Although many studies have focused on PBF-LB of titanium alloys [5, 7, 20], there is limited information on PBF-LB of β-21S and its response to post-process heat treatment. Pellizari et al. [21] reported near fully dense PBF-LB β-21S, consisting of elongated β-phase with UTS of 831 MPa and 21% elongation, and no heat treatment study was conducted. To fill this knowledge gap, in this research, the mechanical behavior of the AB and STA β-21S alloys produced by PBF-LB was investigated. Tensile properties and hardness were measured for both alloys. The resulting mechanical properties conducted at RT and at 450 °C were correlated with the microstructure, assessed by scanning electron microscopy (SEM), and optical microscope (OM).

2 Materials and methods

β-21S powder, sourced from GKN Powder Metallurgy, was used. Table 1 shows the composition as specified by the certificate of conformity provided by the supplier.

Figure 1 shows the powder morphology that was mostly spherical with a few satellites. The particle size distribution (PSD) was measured using LA-920 Horiba laser particle size analyzer. Figure 2a shows the PSD of the powder with a D10, D50 and D90 of 32, 45 and 70 μm, respectively. Powder flowability analysis was conducted using the GranuDrum apparatus. The cohesive index (CI) value as a function of rotational speed is shown in Fig. 2b. The measured values ranged between 13 and 19 for rotating speeds up to 30 rpm. Literature has shown that powder with lower cohesive index possesses better flowability [22], with a critical CI of 24 to maximize powder spreading quality for powder bed processing [22].

Rectangular prism samples with dimensions of 80 mm × 10 mm × 10 mm were manufactured using a Renishaw AM400 PBF-LB machine equipped with a 400 W pulsed Nd:YAG. To prevent oxidation, the process was conducted under Ar atmosphere, and the O_2 was kept below 300 ppm throughout the print. Ti–6Al–4 V (wt%) standard set of parameters provided by Renishaw was used with scanning strategy of 67° rotation per layer.

The heat treatment consisted of a β-solution treatment at 850 °C (above β-transus, ∼ 805 °C [14]) for 0.5 h, air cooled (AC); then aged at 538 °C for 8 h followed by AC. A schematic representation of the heat treatment schedule is presented in Fig. 3.

Table 1 Chemical composition of β-21S powder from the certificate of conformity of the supplier

Element	Mo	Al	Nb	Si	O	C	H	N
Wt%	15	3.2	2.7	0.2	0.17	0.05	0.02	0.05

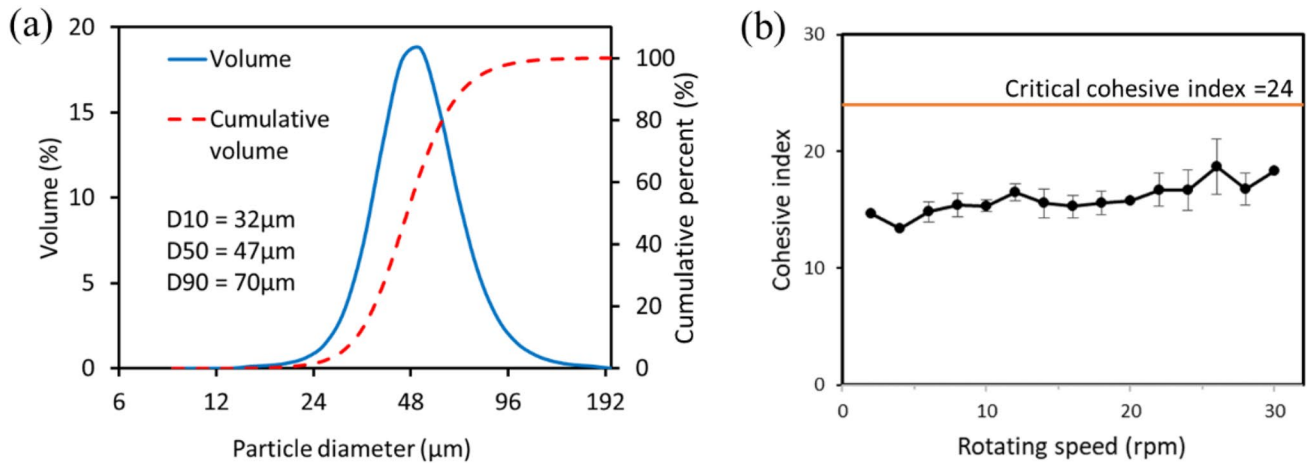**Fig. 1** SEM micrographs showing the size, shape and morphology of the β-21S particles
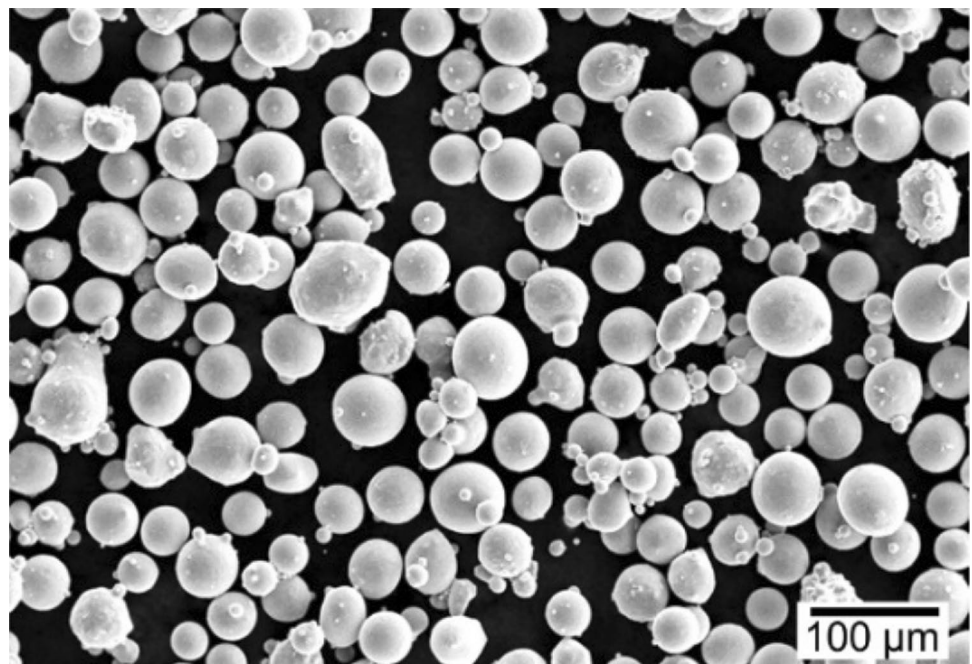
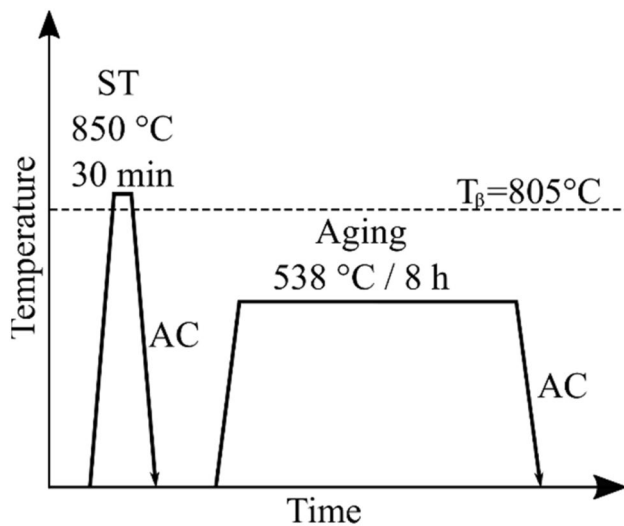Fig. 2 **a** Particle size distribution and **b** cohesive index of Ti β-21S

Fig. 3 Schematic of the heat treatment tested in this study

Phase analysis was conducted for both, AB and STA samples, using a Bruker D8 Discovery X-Ray Diffractometer (XRD) with a copper source ($\lambda = 1.5406$ nm). The XRD was performed in the range of 20°–100° in 2θ using four frames and 300 s per frame. The AB and STA samples were sectioned along the build direction (BD) for microstructural examination and prepared following a standard metallographic procedure. Grain morphology, texture, and phase map in the AB condition were analyzed by electron backscattered diffraction (EBSD) system using a Hitachi SU3500 SEM. The operating conditions were 15 kV and 0.2 μm step size. Aztec data acquisition software combined with the HKL Channel 5 data processing software was used for the EBSD data analysis. The microstructure was revealed using Kroll's etchant (91% deionized water (H_2O), 6% nitric acid

(HNO$_3$) and 3% hydrofluoric acid (HF)). For optical imaging, a Nikon light optical microscope (OM) equipped with a Clemex Vision System was used. The relative density as well as the volume percentage of the α-phase was obtained using image analysis software Image J [23]. Experimental density was measured by the Archimedes' principle. A Hitachi 3500 SEM equipped with energy dispersive spectrometer (EDS) was used for detailed microstructural analysis.

Vickers microhardness analysis was performed on a CM-100AT Clark microhardness indenter using 200 gf load and a dwell time of 15 s. Ten independent measurements were done within each sample and averaged. Tensile tests were carried out at RT and at 450 °C using a TestResources 313Q electromechanical test machine with a constant crosshead speed (0.75 mm/min), resulting in a strain rate of 6.7×10^{-4}/s (gauge length of 12.5 mm). Fractography analysis was conducted on the tested samples with a Hitachi 3500 SEM.

3 Results

3.1 Microstructural characterization of AB

The density measurement as well as the microstructure analyses of the AB alloy were carried on a plane parallel to the BD as indicated in the schematic in Fig. 4a. Figure 4b shows a mosaic of micrographs of an AB sample used to measure the relative optical density through image analysis. An average relative density of 99.9% was measured. While a density of 4.92 g/cm^3 was obtained using Archimedes' principle, which is 99.8% in relation to the reference density value established for the alloy, 4.93 g/cm^3 [24]. Few near-spherical in morphology and randomly distributed pores associated with gas entrapment from the

Fig. 4 **a** Schematic illustrations of the plane used for micro-structural analysis. **b** Optical image showing the relative density in AB condition
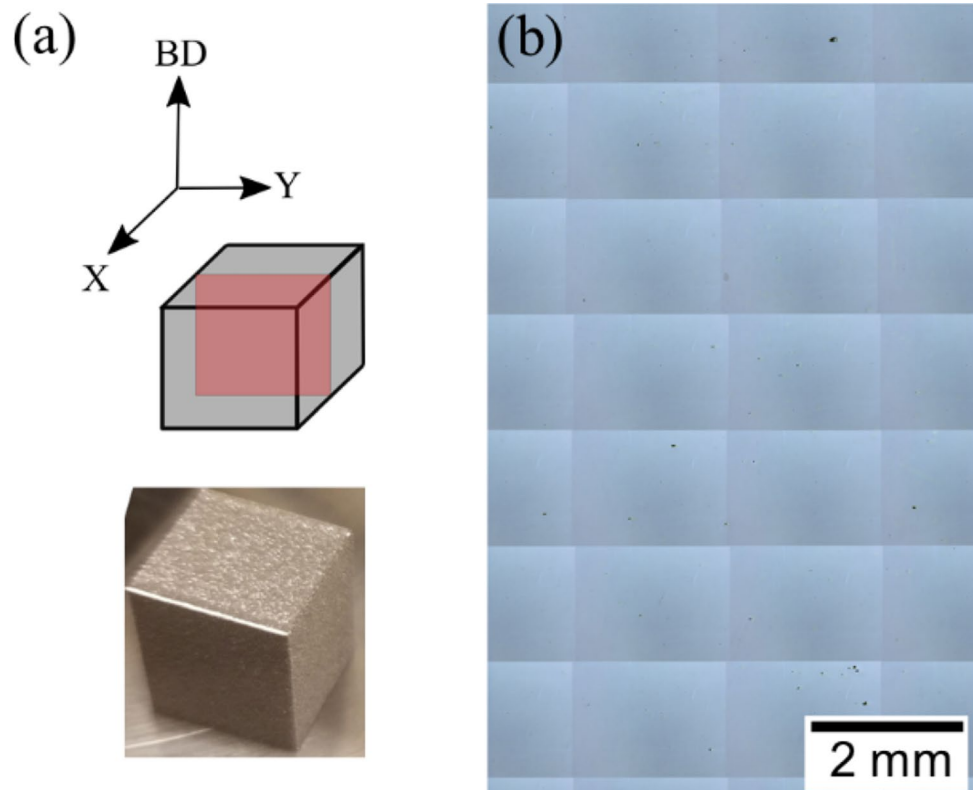
shielding Ar gas atmosphere during processing [2] were observed within the sample.

Figure 5a depicts the XRD pattern of the AB sample. The XRD suggests the presence of a single β-phase, which matches PDF 04-020-9142 [25].

The molybdenum equivalency (MoE) value of 12.84 for β-21S calculated using the Eq. (1) [26] supports the observation of a β-phase at RT as reported by Ivasishin et al. [27]. In general, a MoE value of approximately 10.0 is required to stabilize the β-phase when cooling from above the beta transus temperature.
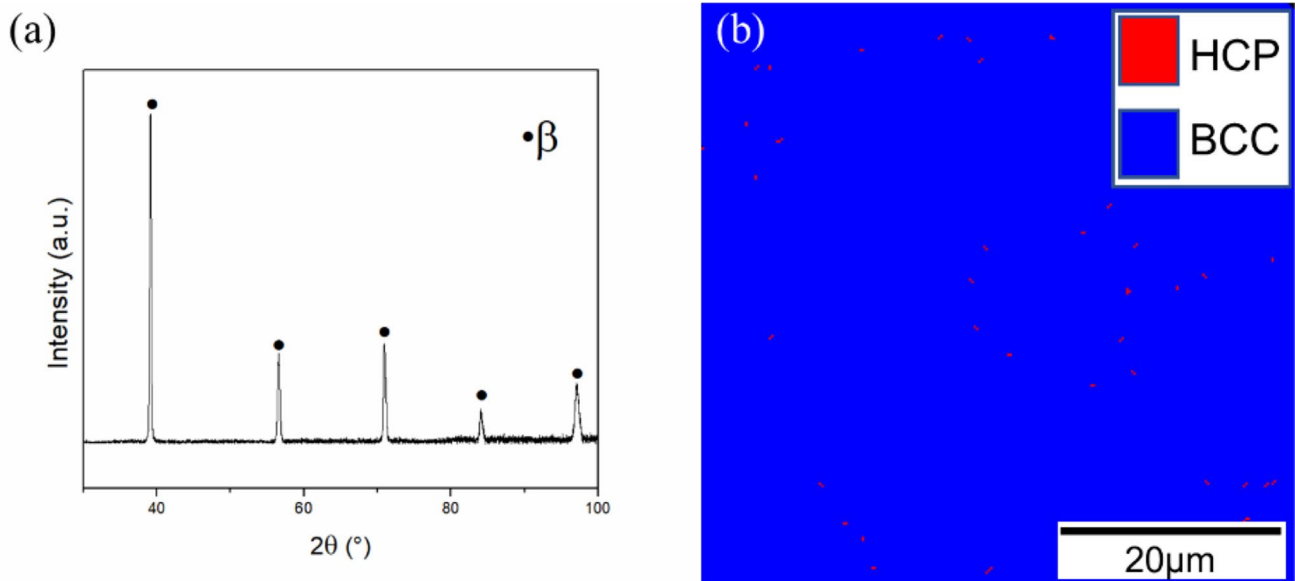
Fig. 5 **a** XRD, **b** phase map of the AB sample

$$MoE = 1.0(wt\% \text{ Mo}) + 0.67(wt\% \text{ V}) + 0.44(wt\% \text{ W}) + 0.28(wt\% \text{ Nb})$$
$$+ 0.22(wt\% \text{ Ta}) + 2.9(wt\% \text{ Fe}) + 1.6(wt\% \text{ Cr}) + 1.25(wt\% \text{ Ni}) \quad\quad (1)$$
$$+ 1.70(wt\% \text{ Mn}) + 1.70(wt\% \text{ Co}) - 1.0(wt\% \text{ Al}).$$

To further confirm this single β-phase, a phase map using EBSD was obtained and shown in Fig. 5b. The EBSD analysis was performed for BCC and HCP structures, and are represented by blue and red colors, respectively. As shown, the volume fraction of HCP precipitates seems to be extremely low. To get insight on the presence of the precipitates, a continuous cooling transformation (CCT) and isothermal transformation (TTT) diagrams were calculated by TC-PRISMA [28]. Figure 6 presents the CCT and TTT diagrams depicting the onset of α-phase precipitation (volume fraction $=10^{-4}$) in the β-phase matrix. Since the alloy has a solidus temperature of 1401 °C/s, and is subjected to cooling rates in the order of 10^3–10^4 °C/s, which are the common cooling rates in the solid state observed during PBF-LB [29], the CCT diagram was calculated below this temperature, and within this range. The theoretical calculation shows that even the fastest cooling rate associated with PBF-LB is not high enough to suppress the precipitation of α-phase when passing through the solvus. The α-phase was measured from the phase map to be 0.27%; it should be noted that α-phase was not detected in Fig. 5a due to the small volume.

To analyze the microstructure, the samples were observed under OM and SEM after etching. Figure 7a presents an optical micrograph of the AB sample. Molten pool boundaries are clearly visible in the AB state. Since the remelting of layers during PBF-LB affects the molten pool size, the measurements were taken from the top layer only. The average sizes resultant of the width and depth of the molten pool was 124 ± 15 µm and 70 ± 10 µm, respectively. The presence of β columnar grains with a width of 33 ± 26 µm can also be seen to be primarily parallel to the BD. Formation of columnar microstructure during PBF-LB has been reported before for other Ti alloys [20, 30]. During PBF-LB, a large heat flux is created parallel to the BD. The grains grow along the direction of highest thermal gradient [6, 31], and thus, aligning with the BD. Each layer partially re-melts the previous layer, facilitating the grain growth from existing grains, which acts as a driving force for crystal growth in the same orientation. The epitaxial growth has been reported before for AM and is well documented in [6, 31, 32].

Figure 7b shows a SEM micrograph of the same AB sample. The microstructure in the AB state revealed cellular columnar features within the grains that grew across the molten pool boundaries. The cellular sub-grains form parallel to the heat flux, as mentioned before, following the thermal gradients, and perpendicular to the melt pool. Thus, the dendrites grow through epitaxial growth through multiple layers. Mode and size of the solidification structure are

Fig. 6 The calculated CCT and TTT diagrams for β-21S. Blue line: TTT diagram, red line CCT diagram for α-phase with volume fraction of 10^{-4}. Dashed lines indicate the cooling rates 10^4 °C/s and 10^3 °C/s
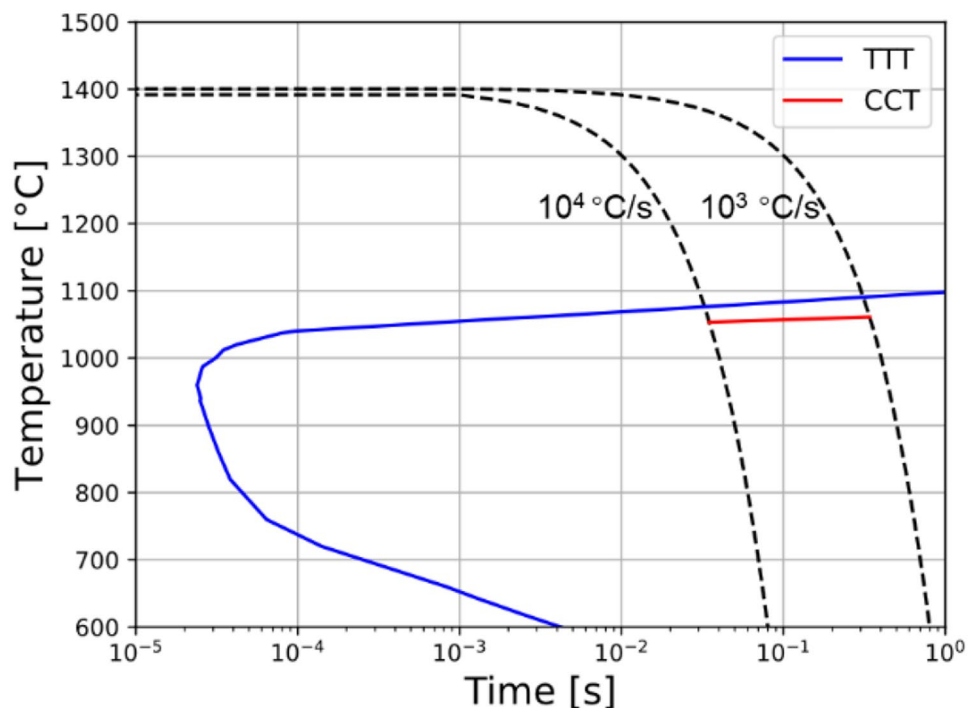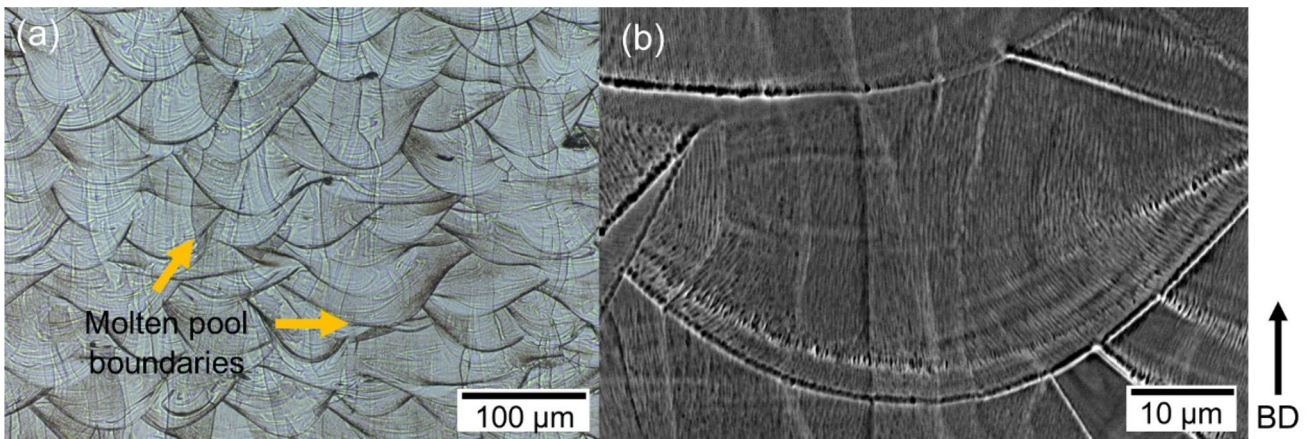
Fig. 7 Images showing the microstructure after etching in AB condition at different magnifications **a** OM, **b** SEM

influenced by the growth rate R (m/s) and the temperature gradient G (°C/m), which are the main solidification parameters. Equiaxed dendrite growth is favored by a lower G/R ratio, while a columnar morphology is favored by higher values of G/R. The high thermal gradient and low growth rate associated with PBF-LB (10^6 °C/m and 0.4 m/s) lead to the formation of columnar dendritic microstructures [6, 33].

The columnar cells within each grain have been reported for numerous materials processed via AM including Ti alloys [20, 34, 35].

Texture was analyzed with EBSD to highlight the preferred crystallographic orientation. Figure 8 presents the EBSD orientation maps, the inverse pole figure (IPF) and pole figures, taken from the cross-sectional view of the AB

Fig. 8 EBSD analysis of the AB sample
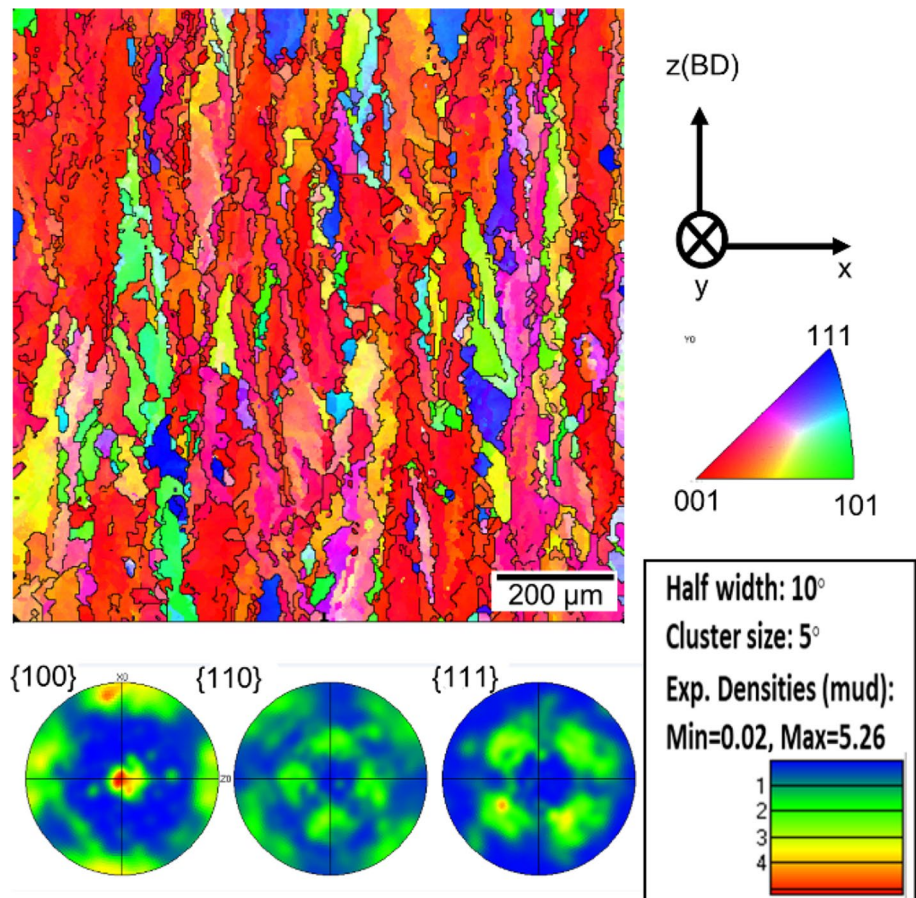
sample. The black lines in the orientation maps denote the high angle grain boundaries (where misorientation > 15°). The microstructure observed is composed of large β-grains, mainly oriented along the building direction, with a preferred <001> alignment. The crystal growth occurs along the maximum temperature gradient, primarily formed parallel to the building direction, in the direction <001>, which is known as the predominant-growth direction for BCC crystals [36, 37] and was also found in PBF-LB of β-21S by Pellizari et al. [21]. Partial re-melting of the previous layers in PBF-LB process facilitates the grain growth from an existing grain, which acts as a driving force for crystal growth in the same orientation [6]. It can be seen from Fig. 8 that the columnar grains propagated several hundreds of microns, larger than the molten pool depth of 70 μm, which confirms the epitaxial growth during PBF-LB.

3.2 Microstructural characterization of STA

Fig. 9 presents the XRD pattern of the STA sample. Peaks corresponding to α-phase (HCP, PDF 04-017-1339 [25]) and β-phase (BCC, PDF 04-020-9142 [25]) were identified. The α-phase is produced by the aging treatment, as discussed before.
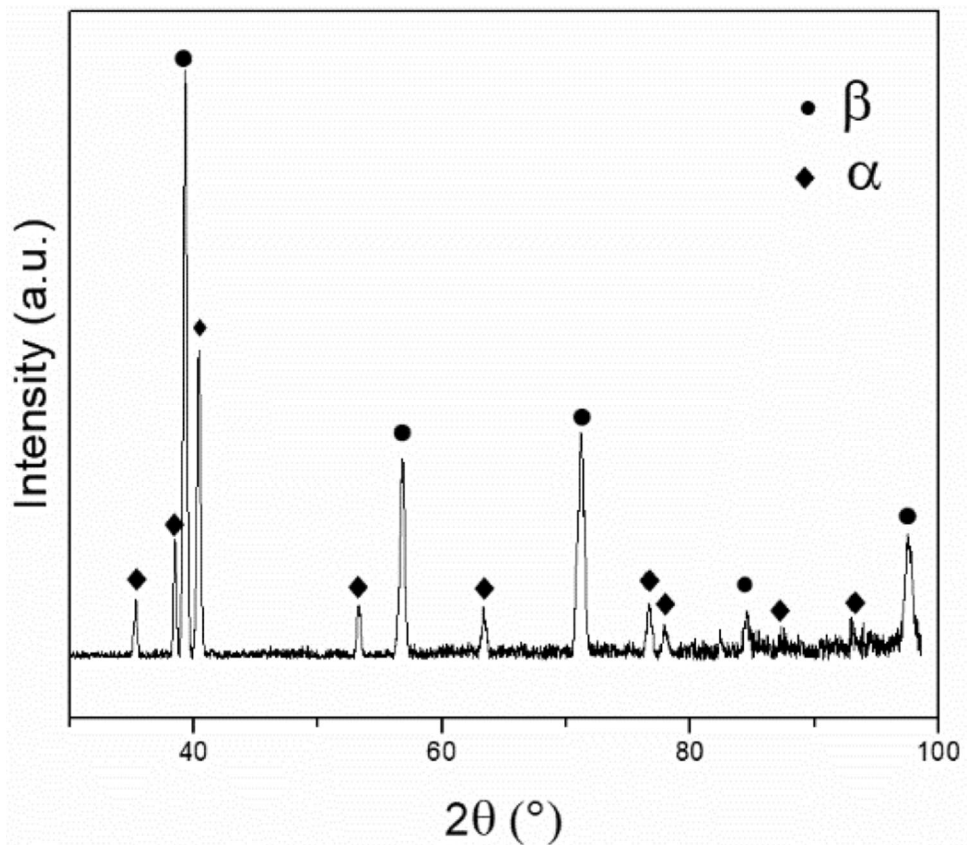
Figure 10 presents SEM micrographs of a sample after STA. As expected, the melt pool boundaries observed in the AB condition are no longer present due to the thermal treatment applied to the sample. The microstructure is composed of β-grains with α-phase at the grain boundaries ($α_{GB}$), α-plates within the grains and a zone free of precipitation (PFZ), indicated by arrows. The measured thickness of the $α_{GB}$ was in the scale of 0.25 ± 0.1 μm. The $α_{GB}$ interdistance was 5 ± 4 μm. The size of the plates was measured to be 1 ± 1 μm and 0.2 ± 1 μm, for length and width, respectively. The explanation for these morphologies is as follows.

During aging, precipitation of α-phase takes place on precursors, and on defect sites, such as grain boundaries, dislocations, and point defects [4, 10, 13]. Grain boundaries are the preferential nucleation sites in diffusional transformations; the formation of $α_{GB}$ occurs as the prior β-grain boundaries serve as nucleation sites of α precipitation [38, 39]. This is due to the fact that defects lower the nucleation barrier for phase nucleation.

At the same time, α-phase will nucleate in the interior of the grains on defect sites, such as vacancies generated during the rapid solidification, and grow into plates. As previously mentioned, Agarwal et al. [19] and Huang et al. [4] reported β-21S produced by non-AM techniques with STA (810–845 °C, 30 min–1 h, AC; 538–540 °C, 8 h, AC) [4, 19]

Fig. 9 XRD pattern STA condition
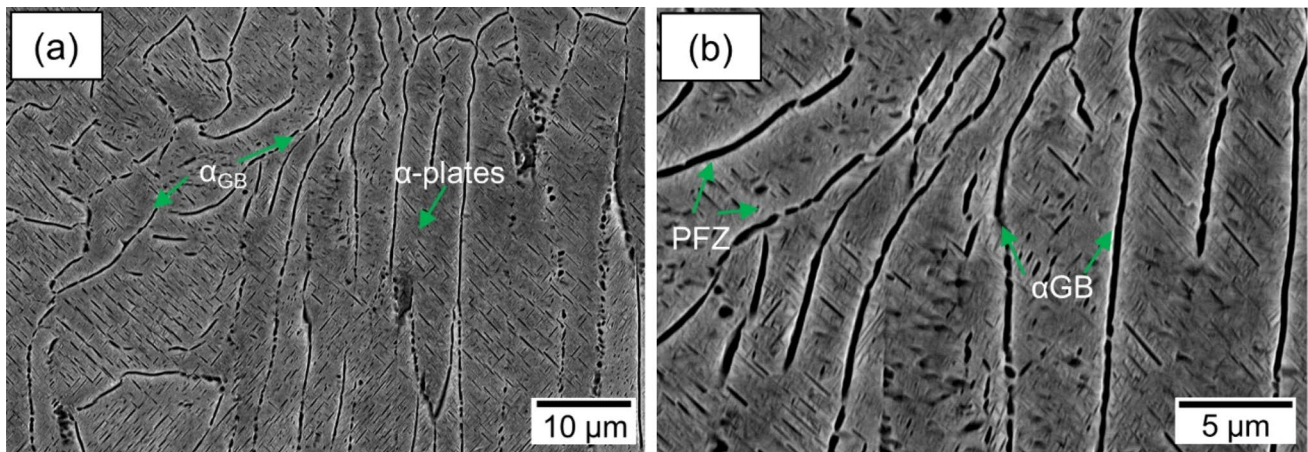
Fig. 10 SEM micrographs showing the microstructure after etching of samples STA at different magnifications

resulted in β hexagonal grains with a stubby morphology of α-phase, while the microstructure obtained in this study with similar STA consisted of columnar β-grains with α-plates of larger size. The difference in the microstructure obtained can be explained by the differences on the manufacturing process. PBF-LB β-21S consisted on uniform β-grains with small percentage of α-phase, while other common manufacturing processes used to produce β-21S involve a deformation process that give rise to a non-uniform microstructure. β-21S microstructure before STA reported by Agarwal et al. and Huang et al. [4, 19] consisted of β-grains with non-uniform recrystallization and larger percentage of second phase, causing more inhomogeneities that give rise to nucleation sites for α-phase during aging. More nucleation sites are beneficial for the precipitation of α-phase but limit its coarsening [40]. Therefore, a more uniform microstructure such as PBF-LB β-21S resulted in lower nucleation sites for the α-phase and extensive growth of α into plates. Another possible explanation can be found by considering that the α-phase is growing from a pre-existing β-phase. This means that incoherence effects, i.e., interfacial energy between the β-matrix and the growing α-phase place a role in the formation of a plate morphology. Further explanation on this is not pursued as it is beyond the scope of this work. In Agarwal et al. and Huang et al. studies [4, 19], the volume fraction of α-phase was measured to be ~33%, while in this study is reported to be ~10%.

The PFZ is explained as follows. The α-phase starts precipitating at grain boundaries during aging, which are preferential nucleation sites, removing solute from the adjacent matrix causing a precipitation depletion zone when aging [4]. A zone free of α-phase has also been reported before in the literature for β-21S in STA [4, 10, 19]. Figure 11a presents high magnification BSE-Comp micrograph of the α-phase in the STA alloy before etching. EDS line scan presented in Fig. 11c shows that the α-phase is enriched in Al

and Ti and depleted in Mo and Nb that are β-phase stabilizers [10].

3.3 Mechanical properties

3.3.1 Hardness

β-21S is normally supplied in β ST condition [26] and used in aged condition. The microhardness obtained in the AB condition was 278 ± 5 HV, similar to the reported value of 274 HV for supplied β-21S ST at 843 °C and AC (no aging) [41].

Our PBF-LB β-21S STA exhibited a value of 380 ± 13 HV. Similar to the reported hardness value for wrought β-21S STA (871 °C, 30 min, AC; 538 °C, 8 h, AC) of 400 HV [42]. As expected, the STA resulted in an increase of microhardness. This is due to the precipitation of the α-phase during the heat treatment; the amount of α/β-phase interfaces increases. Phase interfaces can hinder the dislocations movement, causing the microhardness to increase [43].

3.3.2 Tensile properties AB RT

Figure 12 presents the PBF-LB β-21S YS and UTS as function of elongation in both AB and STA conditions. It also includes some typical values of wrought β-21S ST and STA [18]. The results demonstrate that the PBF-LB β-21S has comparable mechanical properties to the wrought β-21S commonly used in the industry, with higher percentage of ductility attributed to the higher percentage of β-phase [44] presented in PBF-LB β-21S compared with wrought β-21S.

To further analyze these results, fracture surface was observed. Figure 13 presents the tensile fracture surface observed by SEM for the sample in the AB condition tested at RT. The specimen fractured in a ductile manner, as shown in Fig. 13, dimples prevailed in the fracture surface. Dimples

**Fig. 11** EDS line scan of the
STA alloy
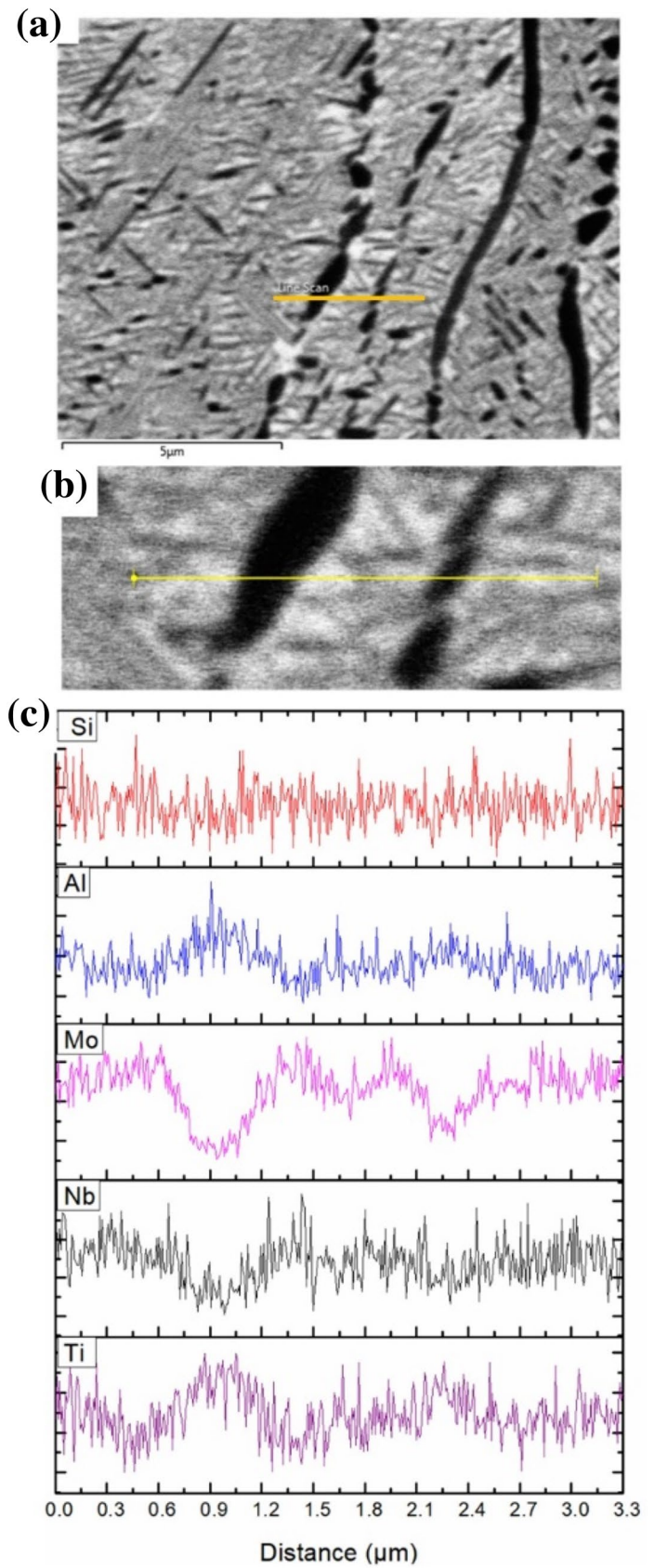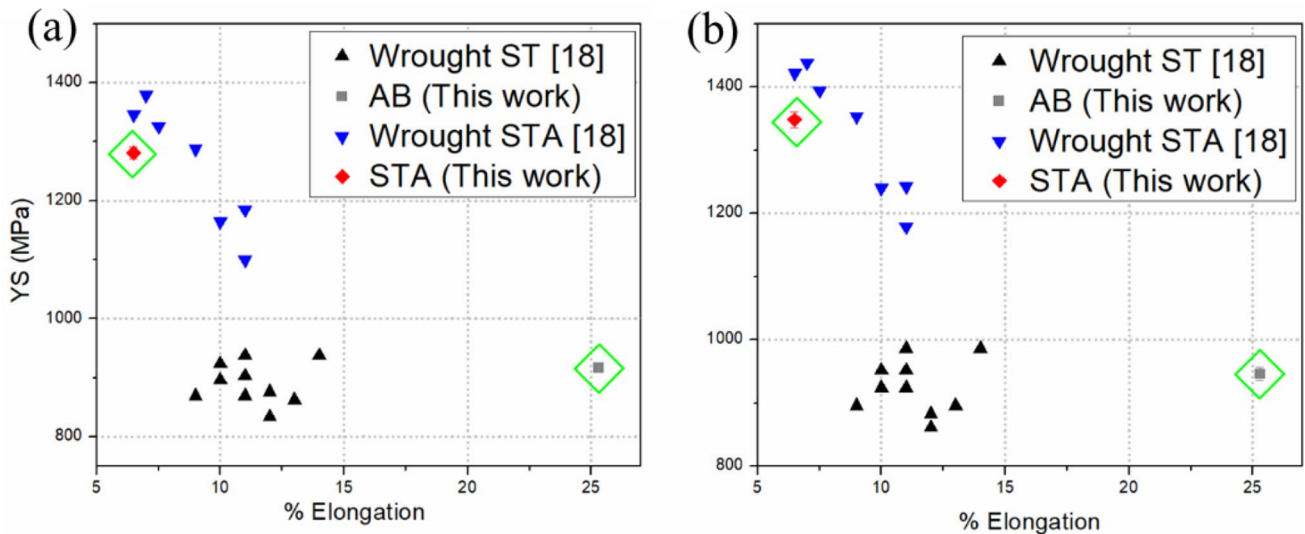
Fig. 12 **a** YS, **b** UTS as a function of elongation at RT. Grey cube and red diamond denoted with green lines represent the values of β-21S in the present study: AB, and STA, respectively. Black trian-

gles pointing up, and blue triangles pointing down represent wrought samples in: ST, and STA, respectively

Fig. 13 SEM micrograph of fracture surface. AB condition
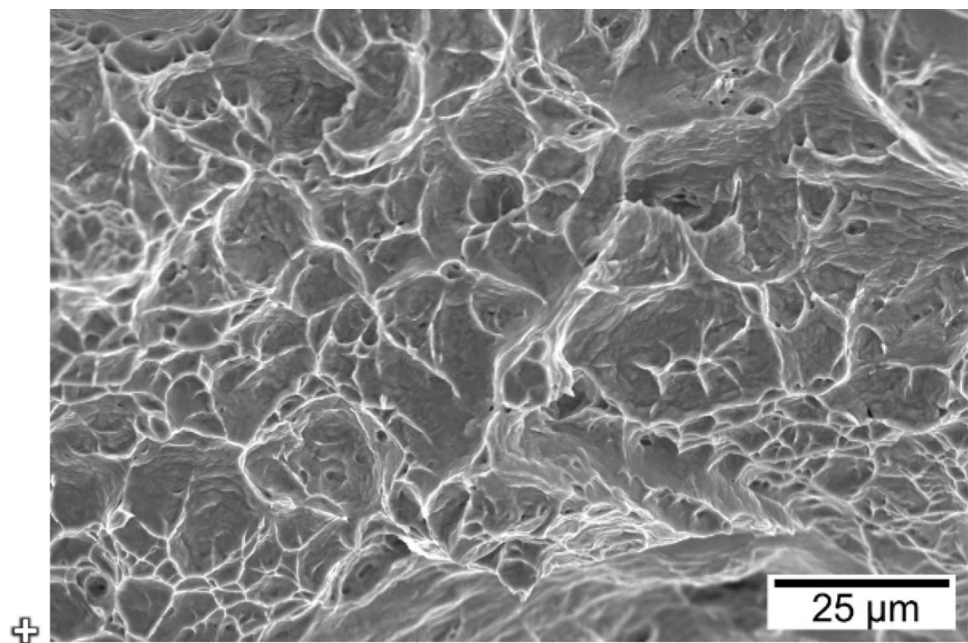
appear with the coalescence of voids formed during plastic deformation, in accordance with the high ductility presented on the AB sample. The observed dimple size of the AB sample was 10 ± 5 μm that can be associated with the β-grain width.

3.3.3 Mechanical properties STA, RT

From Fig. 12, it can be noted that PBF-LB β-21S STA provides competitive results of YS, UTS and elongation

compared to wrought samples. In Fig. 11, it can also be noted that STA of PBF-LB β-21S resulted in an increase of YS, and UTS, with a reduction of ductility. These changes are related to the precipitation of the α-phase. The α-precipitates act as barriers to dislocation slips [43, 45–47], increasing the strength of the alloy while also decreasing the ductility, since they are small and distributed dispersedly within the β matrix. Figure 14 presents the tensile fracture surface of the PBF-LB β-21S STA tested at RT. The fracture surface primarily featured quasi-cleavage facets,

Fig. 14 SEM micrographs of fracture surface at different magnification. STA condition
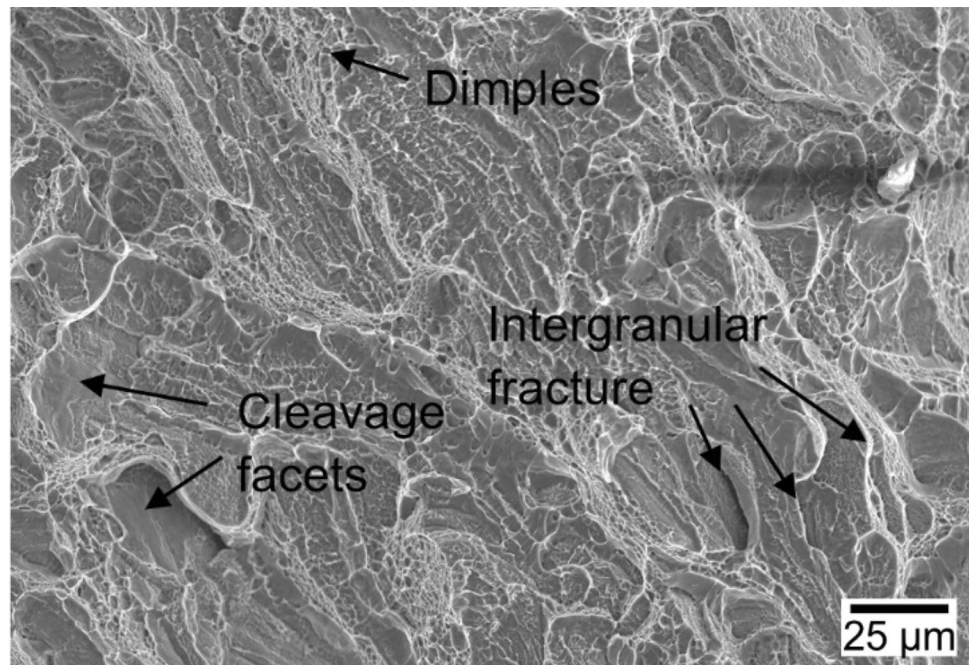
as well as intergranular features. These observations are consistent with the lower ductility presented in the STA, with respect to the AB condition. This result can be related to the microstructure. α_{GB} contributed to the intergranular fracture [48], and at the same time, to reduce the ductility. The α_{GB} provides long soft zones that deform preferentially during deformation causing high stress concentrations and resulted in separation of grains [10, 49, 50]. At the same time, it is suggested by Qin et al. [49] that the transgranular shearing occurs in the region between the tips of two cracks when the crack reaches a critical dimension in β-titanium alloys. On the other hand, dimples of size 1.5 ± 1 μm were also observed, which can be associated with the presence of α-plates, since the interfacial cohesion strength between the α and β-phases can lead to the formation of void at the α/β interface.

3.3.4 Mechanical properties at 450 °C

Non-aged β-alloys are not commercially used at high temperatures as the β-phase prior to aging is metastable and, when exposed to elevated temperatures, is prone to phase transformation and stabilization, altering the properties [19, 51]. Thus, only the sample in STA condition was tested at 450 °C. Figure 15 shows the YS and UTS along with its elongation values for the STA samples from the present work, with comparison to values of the wrought β-21S STA tested at 450 °C [18]. The results obtained are similar to reported typical values as can be seen in the graphs. Compared to PBF-LB β-21S STA tested at RT, testing at 450 °C resulted in reduced YS and UTS, while the percentage of

elongation slightly increased. Increasing temperature is associated with thermally activated processes, such as decrease in dislocation density, that result in reduction of strength at elevated temperatures in Ti alloys [52]. Figure 16 presents SEM micrographs of fracture surface at 450 °C for the STA condition. As can be seen, dimples prevailed along the surface. The dimple size is 2 ± 1 μm, slightly larger than in the STA RT test. Similar to the RT test, void formation can be formed at the α/β interface. It is suggested that void growth occurred with increasing test temperature, while the difference in strength between the β-grain and α_{GB} decreased [53], diminishing the effect of α_{GB} on intergranular fracture. This behavior agrees with the small increase in ductility and reduction in strength presented at increased testing temperature.

4 Conclusions

β-21S alloy samples were produced by PBF-LB. No second phase was detected by XRD and OM, and only β-phase was observed in the as-built condition. Further examination under EBSD demonstrated a small percentage of a α-phase. The crystallographic texture of the β-phase was analyzed. The preferential {001} <100> crystallographic orientation and the formation of elongated grains along the building direction were observed. The samples presented a microhardness of 278 ± 5 HV, YS of 917 ± 1 MPa, UTS of 946 ± 19 MPa, and high ductility ($25.3 \pm 3\%$), which are comparable properties to β-21S produced by non-AM techniques with posterior ST. The β solution treating of
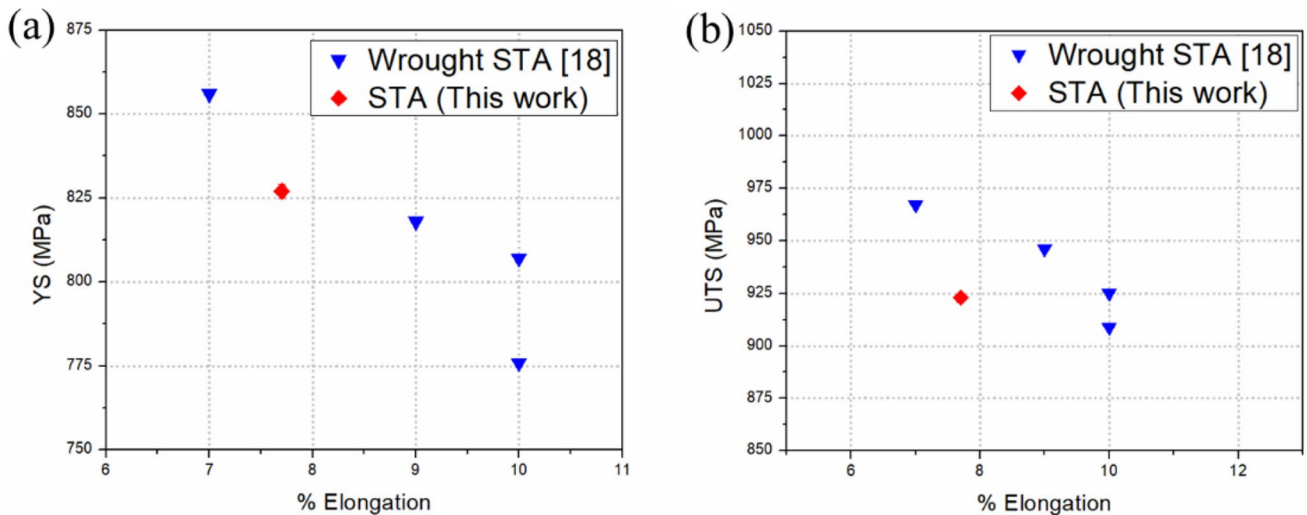
Fig. 15 **a** YS, **b** UTS as a function of elongation at 450 °C. Red diamonds represent the values of β-21S STA in the present study. Triangles represent wrought samples in STA condition

Fig. 16 SEM micrographs of fracture surface at 450 °C, STA condition
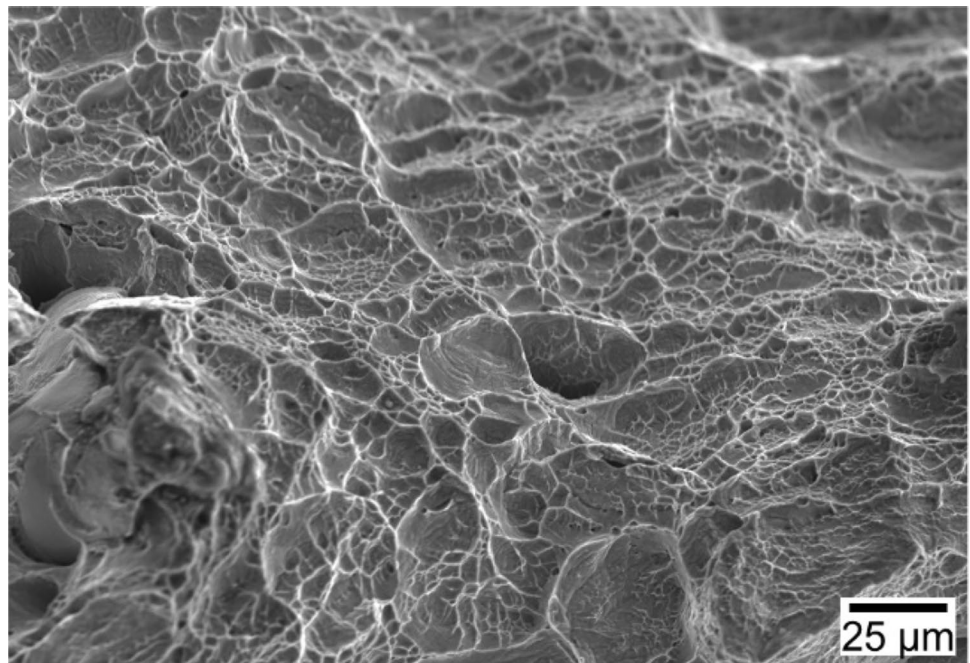
the sample at 850 °C for 30 min and subsequent aging at 538 °C for 8 h, both with AC, caused an increase in microhardness to 380 ± 13 HV, YS to 1281 ± 6 MPa, and UTS to 1348 ± 4 MPa and reduced ductility to $6.5 \pm 1\%$ due to the precipitation of α-phase. At elevated temperature (450 °C), the heat-treated alloy presented a YS of 827 MPa, UTS of 923 MPa and a ductility of 7.7%.

This work has shown that metastable β-21S Ti alloy is a promising candidate material for additive manufacturing processes with properties behaving according to the traditional heat treatment schedule.

Future research on PBF-LB might extend the explanations of α-precipitation on the AB condition. In addition, studies considering different aging time might prove an important area for future research to better understand the α-precipitation after STA.

Declarations

Conflict of interest On behalf of all authors, the corresponding author states that there is no conflict of interest.

References

1. Dirk Herzog VS, Wycisk E, Emmelmann C (2016) Additive manufacturing of metals. Acta Mater 117:371–392. https://doi.org/10.1016/j.actamat.2016.07.019

2. Sanchez-Mata O, Muñiz-Lerma JA, Wang X, Atabay SE, Shandiz MA, Brochu M (2020) Microstructure and mechanical properties at room and elevated temperature of crack-free Hastelloy X fabricated by laser powder bed fusion. Mater Sci Eng A 780:139177. https://doi.org/10.1016/j.msea.2020.139177

3. Wang X, Muñiz-Lerma JA, Sanchez-Mata O, Atabay SE, Attarian Shandiz M, Brochu M (2020) Single-crystalline-like stainless steel 316L with different geometries fabricated by laser powder bed fusion. Prog Addit Manuf 5(1):41–49. https://doi.org/10.1007/s40964-020-00123-9

4. Huang X, Cuddy J, Goel N, Richards NL (1994) Effect of heat treatment on the microstructure of a metastable β-titanium alloy. J Mater Eng Perform 3(4):560–566. https://doi.org/10.1007/BF02645322

5. Kai Dietrich JD, Goff S-L, Bauer D, Forêt P, Witt G (2020) The influence of oxygen on the chemical composition and mechanical properties of Ti-6Al-4V during laser powder bed fusion (L-PBF). Addit Manuf 32:100980. https://doi.org/10.1016/j.addma.2019.100980

6. Sıla Ece Atabay OS-M, Muñiz-Lerma JA, Gauvin R, Brochu M (2020) Microstructure and mechanical properties of rene 41 alloy manufactured by laser powder bed fusion. Mater Sci Eng A 773:138849. https://doi.org/10.1016/j.msea.2019.138849

7. Pazhanivel B, Sathiya P, Sozhan G (2020) Ultra-fine bimodal (α + β) microstructure induced mechanical strength and corrosion resistance of Ti-6Al-4V alloy produced via laser powder bed fusion process. Opt Laser Technol 125:106017. https://doi.org/10.1016/j.optlastec.2019.106017

8. Chaudhuri K, Perepezko JH (1994) Microstructural study of the titanium alloy Ti-15Mo-2.7Nb-3Al-0.2Si (TIMETAL 21S). Metall Mater Trans A 25(6):1109–1118. https://doi.org/10.1007/BF02652286

9. Bania PJ (1991) Next generation titanium alloys for elevated temperature service. ISIJ Int 31(8):840–847. https://doi.org/10.2355/isijinternational.31.840

10. Ian Polmear DS, Nie J-F, Qian M (2017) 7 - Titanium alloys, 5th edn. pp 369–460. https://doi.org/10.1016/B978-0-08-099431-4.00007-5

11. Mantri SA, Choudhuri D, Alam T, Viswanathan GB, Sosa JM, Fraser HL, Banerjee R (2018) Tuning the scale of α precipitates in β-titanium alloys for achieving high strength. Scr Mater 154:139–144. https://doi.org/10.1016/j.scriptamat.2018.05.040

12. Chennakesava Sai Pitchi AP, Sana G, Narala SKR (2020) A review on alloy composition and synthesis of β-Titanium alloys for biomedical applications. Mater Today Proc 26:3297–3304. https://doi.org/10.1016/j.matpr.2020.02.468

13. Malinov S, Sha W, Markovsky P (2003) Experimental study and computer modelling of the β⇒α+β phase transformation in β21s alloy at isothermal conditions. J Alloy Compd 348(1):110–118. https://doi.org/10.1016/S0925-8388(02)00804-6

14. Ivasishin OM, Markovsky PE, Matviychuk YV, Semiatin SL, Ward CH, Fox S (2008) A comparative study of the mechanical properties of high-strength β-titanium alloys. J Alloy Compd 457(1):296–309. https://doi.org/10.1016/j.jallcom.2007.03.070

15. Mantri SA, Choudhuri D, Behera A, Hendrickson M, Alam T, Banerjee R (2019) Role of isothermal omega phase precipitation on the mechanical behavior of a Ti-Mo-Al-Nb alloy. Mater Sci Eng A 767:138397. https://doi.org/10.1016/j.msea.2019.138397

16. Froes FH (2001) Titanium: alloying. In: Buschow KJ, Cahn RW, Flemings MC, Ilschner B, Kramer EJ, Mahajan S, Veyssière P (eds) Encyclopedia of materials: science and technology. Elsevier, pp 9361–9364. https://doi.org/10.1016/B0-08-043152-6/01690-9

17. Chuan Wu MZ (2019) Microstructural evolution, mechanical properties and fracture toughness of near β titanium alloy during different solution plus aging heat treatments. J Alloy Compd 805:1144–1160. https://doi.org/10.1016/j.jallcom.2019.07.134

18. Boyer R, Welsch G, Collings EW (1993) 54. TIMETAL® 21S. Materials properties handbook - titanium alloys. ASM International, United States of America

19. Agarwal N, Bhattacharjee A, Ghosal P, Nandy TK, Sagar PK (2008) Heat treatment, microstructure and mechanical properties of a metastable β titanium alloy timetal® 21s. Trans Indian Inst Met 61(5):419–425. https://doi.org/10.1007/s12666-008-0074-6

20. Kreitcberg A, Brailovski V, Sheremetyev V, Prokoshkin S (2017) Effect of laser powder bed fusion parameters on the microstructure and texture development in superelastic Ti–18Zr–14Nb Alloy. Shape Mem Superelasticity 3(4):361–372. https://doi.org/10.1007/s40830-017-0125-0

21. Pellizzari M, Jam A, Tschon M, Fini M, Lora C, Benedetti M (2020) A 3D-printed ultra-low Young's modulus β-Ti alloy for biomedical applications. Materials 13:2792

22. Yablokova G, Speirs M, Van Humbeeck J, Kruth JP, Schrooten J, Cloots R, Boschini F, Lumay G, Luyten J (2015) Rheological behavior of β-Ti and NiTi powders produced by atomization for SLM production of open porous orthopedic implants. Powder Technol 283:199–209. https://doi.org/10.1016/j.powtec.2015.05.015

23. Schneider CA, Rasband WS, Eliceiri KW (2012) NIH Image to ImageJ: 25 years of image analysis. Nat Methods 9(7):671–675. https://doi.org/10.1038/nmeth.2089

24. William D, Brewer RKB, Wallace TA (1998) Titanium alloys and processing for high speed aircraft. Mater Sci Eng A 243(1):299–304. https://doi.org/10.1016/S0921-5093(97)00818-6

25. Blanton SG-RT (2019) The powder diffraction file: a quality materials characterization database. Powder Diffr 34(4):352–360. https://doi.org/10.1017/S0885715619000812

26. Kolli RP, Devaraj A (2018) A review of metastable beta titanium alloys. Metals 8:506. https://doi.org/10.3390/met8070506

27. Ivasishin OM, Markovsky PE, Matviychuk YV, Semiatin SL (2003) Precipitation and recrystallization behavior of beta titanium alloys during continuous heat treatment. Metall Mater Trans A 34(1):147–158. https://doi.org/10.1007/s11661-003-0216-8

28. Andersson JO, Helander T, Höglund L, Shi P, Sundman B (2002) Thermo-Calc & DICTRA, computational tools for materials science. Calphad 26(2):273–312. https://doi.org/10.1016/S0364-5916(02)00037-8

29. Thampy V, Fong AY, Calta NP, Wang J, Martin AA, Depond PJ, Kiss AM, Guss G, Xing Q, Ott RT, van Buuren A, Toney MF, Weker JN, Kramer MJ, Matthews MJ, Tassone CJ, Stone KH (2020) Subsurface cooling rates and microstructural response

during laser based metal additive manufacturing. Sci Rep 10(1):1981. https://doi.org/10.1038/s41598-020-58598-z

30. Zhao C, Fezzaa K, Cunningham RW, Wen H, De Carlo F, Chen L, Rollett AD, Sun T (2017) Real-time monitoring of laser powder bed fusion process using high-speed X-ray imaging and diffraction. Sci Rep 7(1):3602. https://doi.org/10.1038/s41598-017-03761-2

31. Gäumann M, Henry S, Cleton F, Wagniere JD, Kurz W (1999) Epitaxial laser metal forming: analysis of microstructure formation. Mater Sci Eng A 271(1):232–241. https://doi.org/10.1016/S0921-5093(99)00202-6

32. Dinda GP, Dasgupta AK, Mazumder J (2009) Laser aided direct metal deposition of Inconel 625 superalloy: Microstructural evolution and thermal stability. Mater Sci Eng A 509(1):98–104. https://doi.org/10.1016/j.msea.2009.01.009

33. Vrancken B, Thijs L, Kruth JP, Van Humbeeck J (2014) Microstructure and mechanical properties of a novel β titanium metallic composite by selective laser melting. Acta Mater 68:150–158. https://doi.org/10.1016/j.actamat.2014.01.018

34. Wei Chen CC, Zi X, Cheng X, Zhang X, Lin YC, Zhou K (2018) Controlling the microstructure and mechanical properties of a metastable β titanium alloy by selective laser melting. Mater Sci Eng A 726:240–250. https://doi.org/10.1016/j.msea.2018.04.087

35. Schwab H, Palm F, Kühn U, Eckert J (2016) Microstructure and mechanical properties of the near-beta titanium alloy Ti-5553 processed by selective laser melting. Mater Des 105:75–80. https://doi.org/10.1016/j.matdes.2016.04.10

36. Takeshi Nagase TH, Todai M, Sun S-H, Nakano T (2019) Additive manufacturing of dense components in beta-titanium alloys with crystallographic texture from a mixture of pure metallic element powders. Mater Des 173:107771. https://doi.org/10.1016/j.matdes.2019.107771

37. Sidambe AT, Tian Y, Prangnell PB, Fox P (2019) Effect of processing parameters on the densification, microstructure and crystallographic texture during the laser powder bed fusion of pure tungsten. Int J Refract Met Hard Mater 78:254–263. https://doi.org/10.1016/j.ijrmhm.2018.10.004

38. Yuyong Chen ZD, Xiao S, Lijuan Xu, Tian J (2014) Effect of aging heat treatment on microstructure and tensile properties of a new β high strength titanium alloy. J Alloy Compd 586:588–592. https://doi.org/10.1016/j.jallcom.2013.10.096

39. Furuhara T, Takagi S, Watanabe H, Maki T (1996) Crystallography of grain boundary α precipitates in a β titanium alloy. Metall Mater Trans A 27(6):1635–1646. https://doi.org/10.1007/BF02649821

40. Xu TW, Li JS, Zhang SS, Zhang FS, Liu XH (2016) Cold deformation behavior of the Ti-15Mo-3Al-2.7Nb-0.2Si alloy and its effect on α precipitation and tensile properties in aging treatment. J Alloys Compd 682:404–411. https://doi.org/10.1016/j.jallcom.2016.04.293

41. Wilson T (2017) β21S titanium alloy heat treatment development and improvement. Bachelor of Engineering, University of Queensland

42. George A, Young JRS (1993) Effects of hydrogen on the mechanical properties of a TiMoNbAl alloy. Scr Metall Mater 28(4):507–512. https://doi.org/10.1016/0956-716X(93)90091-6

43. Bei He JL, Cheng Xu, Wang H-M (2017) Brittle fracture behavior of a laser additive manufactured near-β titanium alloy after low temperature aging. Mater Sci Eng A 699:229–238. https://doi.org/10.1016/j.msea.2017.05.050

44. Swee Leong Sing WYY, Wiria FE (2016) Selective laser melting of titanium alloy with 50 wt% tantalum: microstructure and mechanical properties. J Alloy Compd 660:461–470. https://doi.org/10.1016/j.jallcom.2015.11.141

45. Wenguang Zhu QS, Tan C, Li P, Xiao L, Sun J (2020) Tensile brittleness and ductility improvement in a novel metastable β titanium alloy with lamella structure. J Alloy Compd 827:154311. https://doi.org/10.1016/j.jallcom.2020.154311

46. Banerjee D, Williams JC (2013) Perspectives on titanium science and technology. Acta Mater 61(3):844–879. https://doi.org/10.1016/j.actamat.2012.10.043

47. Jiangkun Fan JL, Kou H, Hua Ke, Tang B, Zhang Y (2016) Microstructure and mechanical property correlation and property optimization of a near β titanium alloy Ti-7333. J Alloy Compd 682:517–524. https://doi.org/10.1016/j.jallcom.2016.04.303

48. Chesnutt JC, Froes FH (1977) Effect of α-phase morphology and distribution on the tensile ductility of a metastable beta titanium alloy. Metall Trans A 8(6):1013–1017

49. Dongyang Qin YL, Liu Q, Zheng Li, Zhou L (2013) Transgranular shearing introduced brittlement of Ti–5Al–5V–5Mo–3Cr alloy with full lamellar structure at room temperature. Mater Sci Eng A 572:19–24. https://doi.org/10.1016/j.msea.2013.02.029

50. Dongyang Qin YL, Liu Q, Zhou L (2013) Effects of Si addition on mechanical properties of Ti–5Al–5V–5Mo–3Cr alloy. Mater Sci Eng A 561:460–467. https://doi.org/10.1016/j.msea.2012.10.063

51. Mantri SA, Choudhuri D, Behera A, Cotton JD, Kumar N, Banerjee R (2015) Influence of fine-scale alpha precipitation on the mechanical properties of the beta titanium alloy beta-21S. Metall Mater Trans A 46(7):2803–2808. https://doi.org/10.1007/s11661-015-2944-y

52. Picu RC, Majorell A (2002) Mechanical behavior of Ti–6Al–4V at high and moderate temperatures—part II: constitutive modeling. Mater Sci Eng A 326(2):306–316. https://doi.org/10.1016/S0921-5093(01)01508-8

53. Youngmoo Kim Y-BS, Lee SH (2015) Microstructure and intermediate-temperature mechanical properties of powder metallurgy Ti–6Al–4V alloy prepared by the prealloyed approach. J Alloy Compd 637:234–241. https://doi.org/10.1016/j.jallcom.2015.03.019